

# Physics Informed Viscous Value Representations

Hrishikesh Viswanath<sup>1</sup> Juanwu Lu<sup>2</sup> S. Talha Bukhari<sup>1</sup>  
Damon Conover<sup>3</sup> Ziran Wang<sup>2</sup> Aniket Bera<sup>1</sup>

<sup>1</sup> Department of Computer Science, Purdue University, USA

<sup>2</sup> College of Engineering, Purdue University, USA

<sup>3</sup> DEVCOM Army Research Laboratory, USA

Correspondence to: hv<sub>viswan</sub>@purdue.edu

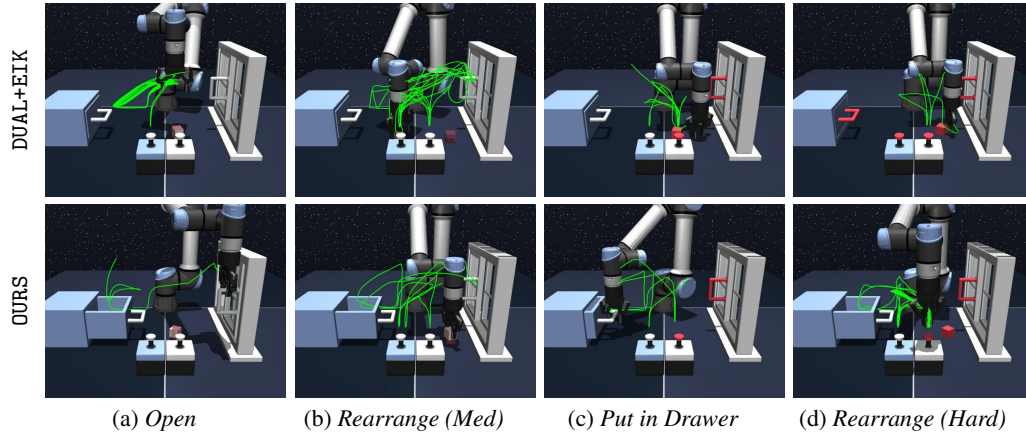


Figure 1: **Efficient manipulation via viscosity-based value functions.** By integrating viscosity based geometric regularization on the value function for *offline goal-conditioned reinforcement learning*, our method successfully executes complex manipulation tasks where the Eikonal baseline [1] struggles. As shown (Bottom), our approach yields direct, stable trajectories across various tasks, overcoming the erratic and suboptimal paths generated by the baseline (Top).

**Abstract:** Offline goal-conditioned reinforcement learning (GCRL) learns goal-conditioned policies from static pre-collected datasets. However, accurate value estimation remains a challenge due to the limited coverage of the state-action space. Recent physics-informed approaches have sought to address this by imposing physical and geometric constraints on the value function through regularization defined over first-order partial differential equations (PDEs), such as the Eikonal equation. However, these formulations can often be ill-posed in complex, high-dimensional environments. In this work, we propose a physics-informed regularization derived from the viscosity solution of the Hamilton-Jacobi-Bellman (HJB) equation. By providing a physics-based inductive bias, our approach grounds the learning process in optimal control theory, explicitly regularizing and bounding updates during value iterations. Furthermore, we leverage the Feynman-Kac theorem to recast the PDE solution as an expectation, enabling a tractable Monte Carlo estimation of the objective that avoids numerical instability in higher-order gradients. Experiments demonstrate that our method improves geometric consistency, making it broadly applicable to navigation and high-dimensional, complex manipulation tasks. Open-source codes are available at <https://github.com/HrishikeshVish/phys-fk-value-GCRL>.

**Keywords:** Physics Informed, Goal-conditioned Reinforcement Learning

# 1 Introduction

Offline goal-conditioned reinforcement learning (GCRL) [2] provides a framework for training agents to reach desired states using static, pre-collected datasets. By leveraging large-scale offline datasets, this paradigm offers potential for real-world applications such as robotic manipulation and autonomous navigation. A key challenge in this setting is accurately estimating the goal-conditioned value functions (GCVF) [2], which serve both as a critic for policy extraction and a guide for planning. While standard value function parameterizations [3, 4, 5] are empirically sufficient, the value iterations rely purely on local reward propagation. As a result, the process lacks the structural inductive biases needed to capture the underlying geometry of the state space, which leads to uninformative or unbounded value estimates, particularly in sparse-reward settings [3, 1].

To enforce the necessary structural bounds, there has been an increasing interest in modeling structured representations with physical and geometric priors, particularly within model-based and Koopman methods [6, 7], while the recent model-free dual-goal approach explicitly models the temporal distance between states [8]. Meanwhile, another promising direction is to leverage physics-informed constraints that regularize the structure of learned functionals by partial differential equations (PDEs) derived from optimal control theory. For instance, methods such as Eik-HIQL [1] leverage the Eikonal equation to model the value function as a geometric distance satisfying a unit-gradient condition.

While PDE constraints have proven effective, they pose specific challenges in complex and stochastic environments. In their essence, these formulations [9, 10, 11, 12, 13] model the shortest paths in continuous spaces and can be ill-posed in high-dimensional planning problems [14]. Another class of approaches directly models the Hamilton-Jacobi-Bellman (HJB) equation [15]. However, this requires knowledge of the system dynamics [15], and solving this can lead to instabilities [16]. A recent work has proposed a stochastic relaxation of the HJB problem, leveraging ideas from stochastic optimal theory, as a tractable approach to reinforcement learning [17]. In the deterministic case, a vanishing viscosity method [18, 14] can be used to define a deterministic HJB viscosity solution as the limit of solutions to the stochastic HJB problem as noise vanishes. Nevertheless, it remains an open question how to adapt these techniques for learning GCVF in an offline model-free reinforcement learning setting.

**Our Contributions.** This work aims to investigate whether a viscosity-based formulation of physics constraints, derived from optimal control, can be practically leveraged to improve value estimation without incurring prohibitive computational costs or instabilities. Specifically, we derive a physics-informed (PI) regularization that explicitly bounds updates to value functions during GCRL value iteration, leveraging the necessary and sufficient conditions for optimal control derived from the HJB equation. However, directly computing the PI residual can be computationally intractable, as the viscosity solution to the HJB is a semilinear elliptic PDE. To bypass the direct calculation of unstable higher-order gradients, we adopt linearization techniques and the Feynman-Kac theorem to recast the PDE solution as an expectation, enabling a tractable Monte Carlo estimate of the objective. Finally, we discuss how this formulation compares with the state-of-the-art hierarchical strategy, HIQL [3], and whether physics-informed strategies can comparably solve tasks without hierarchical representations [19].

# 2 Related Works

**Offline Goal-Conditioned Reinforcement Learning.** Goal-conditioned Reinforcement Learning (GCRL) [20, 5, 21] is a class of RL that aims to learn goal-conditioned policies that take actions to achieve the goal state. Early works, such as hindsight goal relabeling, focus on adapting online algorithms to the offline settings [22, 23, 2], while consecutive works leverage techniques like discounting and advantage weighting [24, 25]. Recent offline approaches, including Implicit Q-Learning (IQL) [26] and Implicit Value Learning (GCIVL) [8], enable transitive planning via expectile regression without out-of-sample action queries, but often suffer from the curse of horizon

due to compounding value errors over long trajectories. Hierarchical and horizon reduction methods [3, 19, 27] mitigate this by decomposing tasks into sub-goals or using  $n$ -step value estimates. Meanwhile, quasimetric and contrastive learning approaches incorporate geometric properties in their architectures [28, 29]. However, most existing methods directly learn value functions from data without explicit physical priors. This purely data-driven approach lacks the structural bounds needed to constrain value iteration, leading to biased estimates from bootstrapping and poor generalizability due to insufficient coverage of the state-action transition.

**Physics-Informed Value Regularization.** Regularization of value estimation via physics-informed constraints has gained increasing attention in planning and RL, with prior work enforcing first- or higher-order consistency in value derivatives from an optimal control perspective [30, 16]. Several recent works have incorporated Eikonal constraints into motion planning [12, 13, 14]. While some works model the HJB directly [31, 15], others leverage operator learning to combine neural operators with Eikonal PDEs for motion planning [32]. Among RL methods, recent work includes deriving offline RL objectives from the HJB equation [15] and using Eikonal-based regularization to constrain the value gradient norm for shortest-path navigation [1]. However, such first-order constraints are often ill-posed for high-dimensional, complex problems, leading to numerical instability in neural approximations. Furthermore, by recasting the PDE as an expectation via the Feynman-Kac theorem, our stochastic formulation bypasses the gradient instabilities often observed when explicitly computing higher-order terms [33].

### 3 Preliminaries

In this section, we briefly introduce GCRL, and optimal control. And in Section 4, we discuss how our proposed method is derived by connecting goal-conditioned reinforcement learning to optimal control and viscosity solution to HJB. Readers can find a table of notations in Appendix A for references.

**Goal-conditioned Reinforcement Learning.** Let  $\mathcal{P}(\mathcal{X})$  be a set of valid probability distributions defined on the space  $\mathcal{X}$ . We denote a goal-conditioned Markov decision process (GC-MDP) by  $\mathcal{M} = (\mathcal{S}, \mathcal{A}, p, r)$ , with state space  $\mathcal{S} \subset \mathbb{R}^n$ , action space  $\mathcal{A} \subset \mathbb{R}^m$ , system transition dynamics given by  $p(\mathbf{s}_{t+1} \mid \mathbf{s}_t, \mathbf{a}) : \mathcal{S} \times \mathcal{A} \rightarrow \mathcal{P}(\mathcal{S})$ , and goal-conditioned reward function  $r(\mathbf{s}, \mathbf{g}) : \mathcal{S} \times \mathcal{S} \rightarrow \mathbb{R}$ , where the goal is defined in the state space  $\mathbf{g} \in \mathcal{S}$ . A goal-conditioned policy is denoted as  $\pi(\mathbf{a} \mid \mathbf{s}, \mathbf{g}) : \mathcal{S} \times \mathcal{S} \rightarrow \mathcal{P}(\mathcal{A})$ . GCRL aims to solve for an optimal policy  $\pi^*$  that maximizes the expected cumulative discounted rewards to reach the goal state:  $\pi^*(\mathbf{a} \mid \mathbf{s}, \mathbf{g}) \triangleq \arg \max_{\pi \in \Pi} \mathbb{E}_{\tau \sim p^\pi(\tau)} \left[ \sum_{t=0}^T \gamma^t \cdot r(\mathbf{s}_t, \mathbf{g}) \right]$ , where  $\Pi$  is policy space,  $\tau \triangleq (\mathbf{s}_0, \mathbf{a}_0, \dots, \mathbf{s}_{T-1}, \mathbf{a}_{T-1}, \mathbf{s}_T)$  represents a trajectory,  $p^\pi(\tau)$  is the distribution of such trajectories by executing policy  $\pi$ , and  $T$  is the decision horizon. Finally, we denote a goal-conditioned state value function (GCVF) induced by policy  $\pi$  as:  $V^\pi(\mathbf{s}, \mathbf{g}) \triangleq \mathbb{E}_{\tau \sim p^\pi(\tau \mid \mathbf{s}_0 = \mathbf{s}, \mathbf{g})} \left[ \sum_{t=0}^T \gamma^t \cdot r(\mathbf{s}_t, \mathbf{a}_t, \mathbf{g}) \right]$ .

**GCRL with Optimal Control.** We study a continuous-time dynamical system [34, 35, 36] defined on a state space  $\mathcal{S} \subset \mathbb{R}^d$ ,  $d\mathbf{s}_t = (f(\mathbf{s}_t) + \mathbf{u}_t) dt$  where  $f : \mathcal{S} \rightarrow \mathbb{R}^d$  denotes the uncontrolled drift,  $\mathbf{u}_t \in \mathcal{U} \subset \mathbb{R}^d$  is the control input. We consider the finite-horizon optimal control problem with objective functional  $\mathcal{J}(\tau) = \mathbb{E} \left[ \int_0^T c(\mathbf{s}_t, \mathbf{u}_t) dt + q_f(\mathbf{s}_T, \mathbf{g}) \right]$ , where  $c : \mathcal{S} \times \mathcal{U} \rightarrow \mathbb{R}$  is the running cost and  $q_f : \mathcal{S} \times \mathcal{S} \rightarrow \mathbb{R}$  is the terminal cost. Here, we assume that the cost function is continuously differentiable with respect to any state-control pair  $(\mathbf{s}_t, \mathbf{u}_t) \in \mathcal{S} \times \mathcal{A}$ , which is reasonable in most RL settings. Following [17], we treat the model-free GCRL as a special case of an optimal control problem, with *unknown state transition dynamics*. In the following section, we showcase how to solve the GCRL as a relaxed stochastic control problem in continuous time, drawing inspiration from prior work [37, 38]. Specifically, we demonstrate that this can be achieved with a plug-and-play value-space regularizer, which improves both the performance and numerical stability in value estimates.

## 4 Learning Value Representations

In this section, we discuss a physics-informed value representation regularized by optimal control physics. Section 4.1 derives the optimal condition given by the Hamilton-Jacobi-Bellman (HJB) equation for the optimal control problem. To mitigate the shortcomings of first-order HJB, recent works [14] consider the vanishing viscosity formulation, which is shown to be smooth and unique. This can be viewed as the deterministic analogue to the second-order HJB formulation used in stochastic optimal control. We derive this in Section 4.1. For computational tractability, we discuss our linearization strategy in Section 4.2 to solve the HJB equation and transform it as a physics-informed regularization in the value function space in Section 4.3.

### 4.1 Solution to Optimal Control

Upon time discretization of the controlled dynamics, the continuous-time control input induces a discrete-time Markov decision process. We denote the resulting action by  $\mathbf{a}_t$  and the corresponding policy by  $\pi$ . Based on the optimality principle [39, 40], the targeted state value function  $V^*(\mathbf{s}, \mathbf{g})$  in a GCRL corresponding to the optimal policy  $\pi^*$  is given by the minimum expected cumulative cost to reach the goal state  $\mathbf{g}$  starting from state  $\mathbf{s}$ , specifically,

$$V^*(\mathbf{s}, \mathbf{g}) \triangleq \min_{\pi \in \Pi} \mathbb{E}_{\tau \sim p^\pi(\tau | \mathbf{s}_0 = \mathbf{s})} \left[ \int_{t=0}^T c(\mathbf{s}_t, \mathbf{a}_t) dt + q_f(\mathbf{s}_T, \mathbf{g}) \right]. \quad (1)$$

Given a system dynamics as specified by Section 3, the sufficient and necessary condition for the optimality of a control is then characterized by the Hamilton-Jacobi-Bellman (HJB) equation [41, 42]. Herein, the optimal control satisfies

$$0 = \min_{\mathbf{a}} [c(\mathbf{s}_t, \mathbf{a}_t) + (f(\mathbf{s}_t) + \mathbf{a}_t)^\top \nabla V^*(\mathbf{s}, \mathbf{g})], \quad (2)$$

where we invoke the vanishing viscosity solution [18, 14] to add a Laplacian term  $\nu \Delta V$ , where  $\nu$  is a small scaling factor. We denote the resulting Hamiltonian as  $H(\mathbf{s}_t, \mathbf{a}_t, \nabla V^*, \Delta V^*)$  and  $\Delta V = \text{Tr}(\nabla^2 V)$ . We note the similarity between this form and the second-order HJB used in stochastic optimal control [43, 36]. Under ideal conditions (i.e., an infinite sample budget and on-policy data), the Q-learning frameworks used in GCRL converge to the ideal value function. However, these are often violated in the offline setting, where datasets are biased and long-horizon tasks lead to extrapolation errors. Furthermore, the function dynamics  $f(\mathbf{s}_t, \mathbf{a}_t)$  in these settings are unknown, thus resulting in a special case of isotropic dynamics [1]. In such cases, the Hamiltonian in equation 2 provides geometric inductive bias to the learned value function. To simplify the Hamiltonian, we approximate the cost functional  $c(\mathbf{s}_t, \mathbf{a}_t)$  using second-order Taylor expansion to get  $q(\mathbf{s}) + \frac{1}{2} \|\mathbf{a}\|_2^2$ , where following [44],  $q(\mathbf{s}_t)$  denotes state-dependent cost. Solving equation 2 to find the minimizer of  $\mathbf{a}$  yields an optimal policy  $\pi^*(\mathbf{a} | \mathbf{s}) := \mathbf{a} = -\nabla V^*(\mathbf{s})$ . Substituting this in equation 2 gives the Hamiltonian residual under optimal policy (See derivation in Section B.1):

$$H(\mathbf{s}, \mathbf{a}^*, \nabla V^*, \Delta V^*) = q(\mathbf{s}) - \frac{1}{2} \|\nabla V^*(\mathbf{s}, \mathbf{g})\|_2^2 + \nu \Delta V^*(\mathbf{s}, \mathbf{g}) \quad (3)$$

### 4.2 Linearization

Solving the Hamiltonian, defined in equation 3, remains a challenge due to the computational intractability of computing higher-order gradients in high-dimensional settings. To tackle this challenge, we exploit the property of this formulation that it admits a closed-form linearization via the Cole-Hopf transformation [17].

**Cole-Hopf Transformation.** *The Cole-Hopf transformation is a change-of-variables for linearization of the value function given by  $\Psi(\mathbf{s}) = \exp(-V(\mathbf{s})/2\nu)$ . Herein, the transformed function  $\Psi$  satisfies a linear PDE.*

We substitute the logarithmic transformation  $V(\mathbf{s}, \mathbf{g}) = -2\nu \log \Psi(\mathbf{s}, \mathbf{g})$  into the Hamiltonian in equation 3 to derive the equivalent linear operator. This results in the residual for the Hamiltonian  $H_{\text{lin}}(\mathbf{s}, \mathbf{a}^*, \Psi^*) = q(\mathbf{s}) - 2\nu^2 \Delta \Psi^*(\mathbf{s}, \mathbf{g}) / \Psi^*(\mathbf{s}, \mathbf{g})$ . We present the derivation in Section B.2.

Since the optimal policy is given by the negative gradient of the optimal state value, minimizing the above residual poses an inductive bias to the physical structure of state and action spaces specified by the state dynamics PDE. However, computing the Laplacian in high-dimensional state spaces (e.g., in settings with high degrees of freedom (DoF), such as the scene-play) is computationally intractable. Meanwhile, recent work [33] has shown that PINNs can suffer from gradient instabilities when handling higher-order gradients. To avoid explicit Laplacian evaluation, we invoke the Feynman-Kac representation of the resulting linear PDE. This recasts the value function as an expectation over trajectories, which can be estimated via Monte Carlo sampling.

### 4.3 Value Function Regularization

Combining equation 2 and the linearized Hamiltonian residual, given  $\nu > 0$ , the linearized solution to the HJB equation is

$$\frac{1}{2\nu^2} q(\mathbf{s}) \Psi^*(\mathbf{s}, \mathbf{g}) - \Delta \Psi(\mathbf{s}, \mathbf{g}) = 0 \quad (4)$$

We can apply the Feynman-Kac formula to express  $\Psi^*(\mathbf{s}, \mathbf{g})$  as a conditional expectation of the next state  $\mathbf{s}'$ . In discrete space, the expectation over  $\mathbf{s}'$  corresponds to a one-step Markov transition (i.e., a random step) whose variance is controlled by  $\nu$  and the time step  $\Delta t$ . We particularly set the running cost  $q(\mathbf{s})$  as an inverse function of the speed profile  $S(\mathbf{s})$ , following the implementation in [1], we set a constant speed of  $S(\mathbf{s}) = 1$  and  $\Delta t = 1$ , reducing the hyperparameter space to  $\nu$ .

**Feynman-Kac Formula.** We consider a 1-step update defined over a small  $\Delta t$ , such that the solution of equation 4 admits the stochastic representation

$$\Psi(\mathbf{s}_t, \mathbf{g}) = \exp(-q(\mathbf{s}_t) \Delta t / 2\nu^2) \mathbb{E}_{\mathbf{s}' \sim p(\mathbf{s}_{t+\Delta t} | \mathbf{s}_t, \mathbf{a})} [\Psi^*(\mathbf{s}', \mathbf{g})] \quad (5)$$

where  $p(\mathbf{s}_{t+\Delta t} | \mathbf{s}_t, \mathbf{a})$  is the state transition dynamics. Essentially,  $\mathbf{s}'$  is the one-step endpoint for a random walk in  $\mathcal{S}$  from  $\mathbf{s}_t$ . In practice, this state-sampling is done by perturbing  $\mathbf{s}_t$  with Gaussian noise.

Applying the log transform to equation 5 and invoking Jensen’s inequality yields an upper bound on the expected optimal value (Section B.3):

$$V^*(\mathbf{s}, \mathbf{g}) \leq \mathbb{E}_{\mathbf{s}' \sim p(\mathbf{s}' | \mathbf{s}, \mathbf{a})} V^*(\mathbf{s}', \mathbf{g}) + q(\mathbf{s}) \Delta t / \nu. \quad (6)$$

$$\mathcal{L}_{\text{phy}}(\boldsymbol{\theta}) \triangleq \mathbb{E}_{\mathbf{s} \sim \mathcal{B}} \left[ \max(0, V(\mathbf{s}, \mathbf{g}; \boldsymbol{\theta}) - \mathbb{E}_{\mathbf{s}' \sim p(\mathbf{s}' | \mathbf{s}, \mathbf{a})} [V(\mathbf{s}', \mathbf{g}; \bar{\boldsymbol{\theta}})] - q(\mathbf{s}) \Delta t / \nu)^2 \right] \quad (7)$$

where  $V(\cdot; \boldsymbol{\theta})$  is the value function to learn and  $V(\cdot; \bar{\boldsymbol{\theta}})$  is a target network to stabilize the expectation estimate. In practice, we compute the expectation over  $\mathbf{s}'$  using Monte-Carlo integrals. To ensure that the process never generates kinematically invalid out-of-distribution (OOD) states, we clip the jump magnitude. Specifically, the sampled state is defined as  $\mathbf{s}' = \mathbf{s} + \min(\nu, d_{\partial \mathcal{X}}) \boldsymbol{\epsilon}$ , where  $\boldsymbol{\epsilon} \sim \mathcal{N}(\mathbf{0}, \mathbf{I})$  and  $d_{\partial \mathcal{X}}$  is the maximum permissible distance to the kinematic boundary  $\partial \mathcal{X}$  along the sampled direction. Our loss is used alongside the TD-learning scheme, which enforces a SARSA-like objective [26], whereas our geometric formulation penalizes high-cost transitions while allowing low-cost ones.

## 5 Experiments

In this section, we evaluate the benefits of our proposed stochastic structure on learned value representations on the standard offline goal-conditioned RL benchmark OGBench [45]. We conduct ablation studies to understand the impact of our method. We follow the standard experimental procedures described in [8] for fair comparisons to baseline models. **Tasks and Datasets.** We consider 13 tasks from the OGBench datasets that cover both manipulation and navigation behaviors.

Table 1: **RESULTS ON STATE-BASED TASKS WITH GCIVL.** We compare the success rates across 4 seeds over goal representation learning methods and highlight the impact of stochastic regularization FK on VIB (the strongest general baseline) and Dual Goal backbones.

ENVIRONMENT	ORIG	ORIG-FK	VIB	VIB-FK	VIP	TRA	BYOL	DUAL	DUAL-FK (Ours)
pointmaze-medium	78 ± 8	20 ± 7	69 ± 13	<b>92 ± 6</b>	0 ± 1	3 ± 6	37 ± 7	76 ± 7	<b>96 ± 3</b>
pointmaze-large	52 ± 6	28 ± 4	50 ± 7	<b>80 ± 3</b>	0 ± 0	1 ± 2	22 ± 12	46 ± 6	<b>77 ± 1</b>
antmaze-medium	71 ± 4	61 ± 5	68 ± 4	<b>75 ± 4</b>	31 ± 5	22 ± 15	39 ± 5	<b>75 ± 4</b>	<b>76 ± 5</b>
antmaze-large	16 ± 3	23 ± 2	9 ± 3	26 ± 2	9 ± 2	22 ± 12	11 ± 5	28 ± 11	<b>39 ± 3</b>
antmaze-giant	0 ± 0	0 ± 0	0 ± 0	0 ± 0	0 ± 0	0 ± 0	0 ± 0	0 ± 0	<b>1 ± 0</b>
humanoid-medium	27 ± 3	27 ± 3	24 ± 2	30 ± 3	7 ± 3	21 ± 3	18 ± 5	29 ± 3	<b>34 ± 3</b>
humanoid-large	3 ± 0	4 ± 1	3 ± 1	4 ± 1	1 ± 0	2 ± 1	2 ± 1	3 ± 2	<b>7 ± 2</b>
antsoccer-arena	<b>47 ± 4</b>	41 ± 1	34 ± 4	30 ± 3	2 ± 1	8 ± 2	11 ± 4	31 ± 3	27 ± 1
cube-single	52 ± 3	68 ± 11	<b>90 ± 3</b>	83 ± 4	40 ± 7	40 ± 5	51 ± 11	89 ± 3	<b>91 ± 1</b>
cube-double	35 ± 5	30 ± 4	33 ± 3	<b>59 ± 3</b>	3 ± 2	7 ± 2	6 ± 4	<b>60 ± 4</b>	52 ± 5
scene-play	46 ± 3	52 ± 7	58 ± 1	81 ± 7	23 ± 6	46 ± 6	44 ± 9	72 ± 6	<b>84 ± 5</b>
puzzle-3x3	5 ± 1	8 ± 2	<b>14 ± 3</b>	11 ± 2	3 ± 1	5 ± 1	0 ± 0	5 ± 1	7 ± 2
puzzle-4x4	14 ± 1	25 ± 3	6 ± 3	10 ± 4	1 ± 1	10 ± 3	1 ± 2	23 ± 3	<b>34 ± 2</b>
AVERAGE	34 ± 1	30 ± 4	35 ± 2	45 ± 3	9 ± 1	15 ± 2	19 ± 2	41 ± 2	<b>48 ± 3</b>

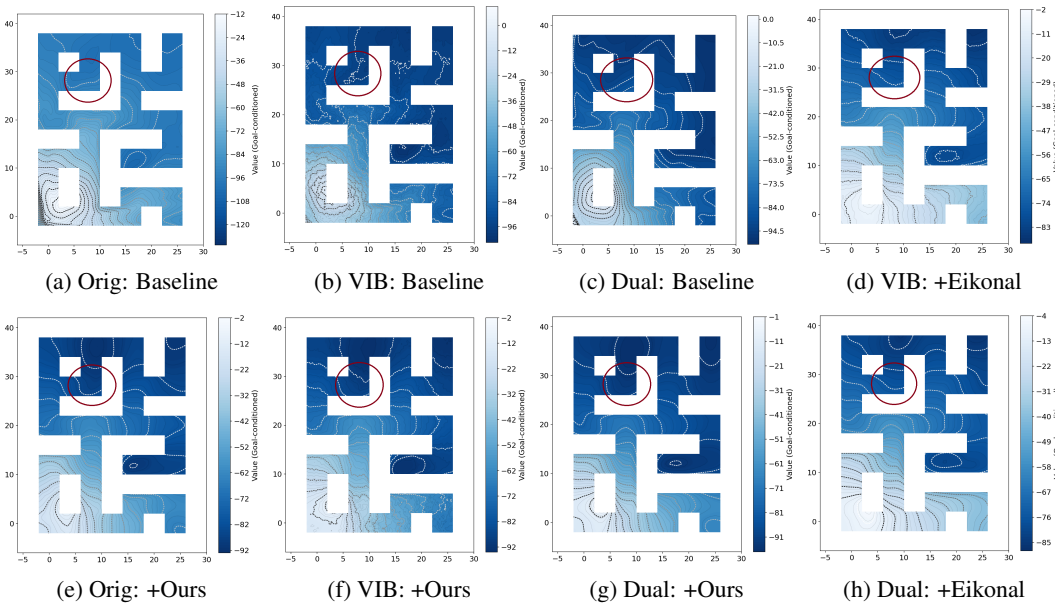


Figure 2: **Qualitative value contour ablation on PointMaze-Large.** Col 1 (Original): Baseline (a) fails globally; ours (e) recovers functional structure. Col 2 (VIB): Baseline (b) exhibits severe jitter; ours (f) significantly stabilizes geometry. Col 3 (Dual): Baseline (c) suffers geometric collapse with contours parallel to paths; ours (g) enforces correct path-orthogonality. Col 4 (Eikonal): While Eikonal constraints (d, h) reduce jitter, they incorrectly align contours parallel to walls. Our viscous formulation strictly preserves orthogonal, geodesic-aligned contours.

The navigation tasks (pointmaze, antmaze, humanoidmaze) focus on navigating a robot through mazes of varying size, each with increasing complexity, with humanoid being the most complex (21 Degrees-of-Freedom in movement). The most complex of these tasks is antsoccer, which involves dribbling a soccer ball to the goal. In the manipulation experiments, we consider cube, scene, and puzzle, which involve a robotic arm manipulating, rearranging, or solving combinatorial puzzles. Furthermore, we consider 32 variants of these tasks, based on size (medium, large, giant) and inference-time complexity (navigate, stitch, teleport).

**Baselines.** Our policy algorithm extends the GCIVL algorithm presented in [8]. We consider 5 representation strategies: Original (i.e., no representations), VIB [46], which trains representations through variational information bottleneck, VIP [4], a metric-based representation, TRA [47], a con-

trastive representation, and BYOL [48], a self-supervised approach. For the physics-informed strategies, we consider the Eikonal regularization EIK from [1].

## 5.1 Results

We present the results on the 13 OGBench tasks in Table 1. We will discuss these results in detail in the following subsections. We will focus on three key questions that will drive our discussion of the ablations.

**Question: Is the proposed regularization dependent on the underlying value representation?**

**Answer:** We evaluate whether our formulation operates independently of the underlying representation (Table 1). While the dual-goal representation performs best, applying our stochastic regularization to the second-best method (VIB) still yields significant improvements. Qualitatively (Figure 2), our physics objective improves value function geometry across representations, aligning contour normals with the geodesic. We also demonstrate policy-agnosticism by integrating our approach with the state-of-the-art hierarchical strategy HIQL (Table 2) and comparing Eik-HIQL against our HIQL-FK.

**Question: Does the proposed formulation alter value function geometry, and how does this impact scalability, robustness, and performance limits compared to Eikonal regularization?**

**Answer:** Visualizing advantage-weighted action probability distributions in pointmaze-large (Figure 4) provides a heuristic for the policy’s preferred movement due to the local geometry of the value function. These fan-shaped visualizations reveal that Eikonal constraints push probability mass toward walls, especially near corners (Figure 4b), whereas DUAL-FK aligns distributions parallel to walls (Figure 4a). In long corridors, our path more closely aligns with the true geodesic. Consequently, while Eikonal struggles in higher-dimensional environments with contact dynamics, DUAL-FK scales favorably to tasks requiring highly nonlinear dynamics such as large-scale stitch and teleport variants, and manipulation tasks involving contact-rich mechanics, constrained domains, and joint angle wraps (e.g., cube-single-play, scene-play), outperforming baselines (Table 2).

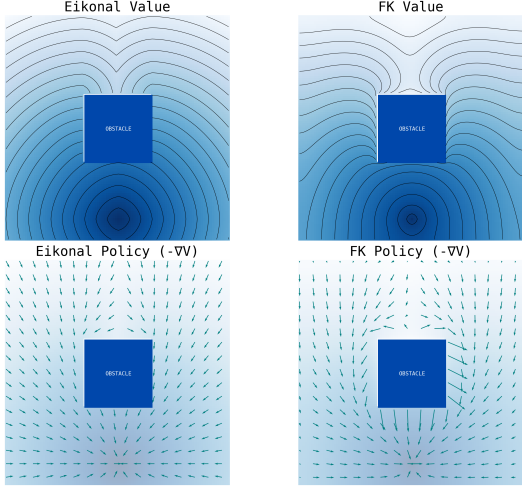


Figure 3: **Toy example with a single obstacle (blue square) in an arena, with the goal state at the bottom:** We analytically solve the exact Eikonal form from [1] and our stochastic HJB PDE (Feynman–Kac) on a toy problem. The second-order HJB PDE produces contours with larger magnitude and curvature near the obstacle, with vectors directed away from it.

Table 2: **ABLATION EXPERIMENTS.** Eik-HIQL applies Eikonal constraint to HIQL policy, DUAL+EIK enforces the first-order Eikonal constraint ( $|\nabla V| \approx 1$ ).

ENVIRONMENT	EIK-HIQL	HIQL-FK	DUAL+EIK	DUAL-FK (OURS)
<i>PointMaze</i>				
point-nav-medium	93 ± 5	95 ± 3	92 ± 1	96 ± 3
point-nav-large	83 ± 9	89 ± 5	79 ± 4	77 ± 1
point-nav-giant	79 ± 13	91 ± 4	73 ± 3	57 ± 7
point-nav-teleport	47 ± 10	45 ± 10	44 ± 2	50 ± 3
point-stitch-medium	96 ± 3	95 ± 2	93 ± 3	93 ± 2
point-stitch-large	73 ± 6	52 ± 10	55 ± 7	30 ± 6
point-stitch-giant	22 ± 10	16 ± 4	30 ± 4	8 ± 3
point-stitch-teleport	43 ± 9	42 ± 3	50 ± 2	52 ± 2
<i>AntMaze</i>				
ant-nav-medium	95 ± 1	97 ± 2	77 ± 4	76 ± 5
ant-nav-large	86 ± 2	92 ± 2	46 ± 3	39 ± 3
ant-nav-giant	67 ± 5	68 ± 3	5 ± 2	1 ± 0
ant-nav-teleport	52 ± 4	50 ± 4	36 ± 1	39 ± 2
<i>HumanoidMaze</i>				
humanoid-nav-medium	86 ± 2	89 ± 2	14 ± 3	34 ± 3
humanoid-nav-large	64 ± 7	46 ± 3	3 ± 2	7 ± 2
humanoid-nav-giant	68 ± 5	4 ± 3	0 ± 0	0 ± 0
<i>AntSoccer</i>				
soccer-nav-arena	19 ± 2	43 ± 3	7 ± 2	27 ± 1
soccer-nav-medium	3 ± 2	6 ± 2	2 ± 1	3 ± 1
soccer-stitch-arena	2 ± 0	13 ± 3	1 ± 1	10 ± 3
soccer-stitch-medium	1 ± 0	4 ± 1	0 ± 0	0 ± 0
<i>Manipulation</i>				
cube-single-play	25 ± 1	26 ± 3	1 ± 0	91 ± 1
scene-play	52 ± 7	56 ± 4	13 ± 2	84 ± 5

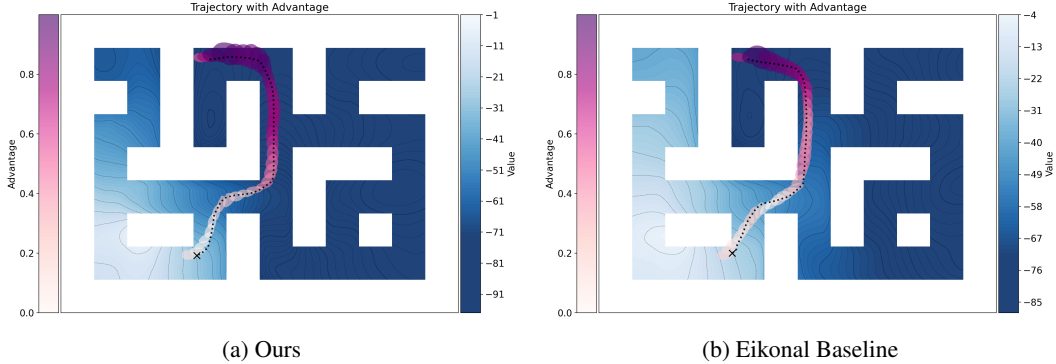


Figure 4: **Comparison of action probability distributions (pink fans) along a trajectory.** (a) **Ours:** The advantage distributions align parallel to the walls, correctly identifying the safe path through corridors. (b) **Eikonal:** The distributions often point directly into walls when the goal is geometrically behind them.

This structural advantage extends to domains with high state uncertainty. In noisy manipulation and puzzle variants (puzzle-3x3, puzzle-4x4) collected with Markovian expert policies and large uncorrelated Gaussian noise, DUAL+EIK fails catastrophically with near-zero success. Conversely, DUAL-FK implicitly incorporates the injected noise into its Feynman-Kac framework, achieving 99% success on cube-single-noisy (Table 3a). We also validate our key hyperparameter choices (Table 3b): performance is robust to sample size, quickly stabilizing for random walk budgets  $K \geq 5$ , while higher Laplacian scales ( $\nu \geq 10^{-2}$ ) are necessary to smooth local minima.

Table 3: **ROBUSTNESS AND SENSITIVITY ABLATIONS.** (a) Ablation on stochastic environments. (b) Showing performance across varying random walk budgets ( $K$ ) and scales ( $\nu$ ).

(a) Noisy environments			(b) Hyperparameters			
ENVIRONMENT	DUAL+EIK	DUAL-FK	<i>Walks</i> ( $K$ )		<i>Scale</i> ( $\nu$ )	
			PARAM	SUCCESS	PARAM	SUCCESS
<i>Noisy Manipulation</i>						
scene-noisy	0 ± 0	53 ± 4			$\nu = 10^{-4}$	55 ± 2
cube-single-noisy	0 ± 0	99 ± 1	$K = 1$	57 ± 3	$\nu = 10^{-3}$	57 ± 3
cube-double-noisy	1 ± 0	30 ± 3	$K = 5$	77 ± 2	$\nu = 10^{-2}$	77 ± 3
<i>Noisy Puzzle</i>			$K = 10$	76 ± 2	$\nu = 10^{-1}$	79 ± 2
puzzle-4x4-noisy	0 ± 0	24 ± 1	$K = 20$	77 ± 2		
puzzle-4x5-noisy	0 ± 0	18 ± 1				

**Limitations.** We characterize the regularizer’s limitations. Much like the baselines, DUAL-FK struggles with massive long-horizon state spaces such as antsoccer-arena or humanoid-large (Table 1), highlighting the limitations of local geometry constraints. However, we observe that the performance improves when used alongside hierarchical policies. Furthermore, in highly stochastic visual domains like Powderworld (Table 6), while perturbing raw pixels space remains unfeasible, enforcing the viscous consistency condition via sampling in the *Impala* encoder’s latent space yields only superficial gains (10% vs 7% on powderworld-hard). Because these embedding spaces are not strictly Euclidean, our physical priors are subject to constraint violations, dampening the effectiveness of the induced value function dynamics.

## 6 Conclusion

We introduced a viscosity-based formulation for physics-informed regularization in Goal-Conditioned RL. This representation-agnostic approach particularly improves upon Eikonal forms in high-dimensional, contact-rich manipulation tasks. Extending this to stochastic pixel domains (powderworld) via latent-space regularization remains a challenge. Future work will explore latent manifold-aware regularization to better preserve latent geometry and recover the robustness seen in state-based tasks. Ultimately, these findings establish viscous regularization as an effective and versatile physical prior for continuous control.

## Acknowledgment

This material is based upon work supported in part by the DEVCOM Army Research Laboratory under cooperative agreement W911NF2020221.

## References

- [1] V. Giammarino, R. Ni, and A. H. Qureshi. Physics-informed value learner for offline goal-conditioned reinforcement learning. *arXiv preprint arXiv:2509.06782*, 2025.
- [2] R. Yang, Y. Lu, W. Li, H. Sun, M. Fang, Y. Du, X. Li, L. Han, and C. Zhang. Rethinking goal-conditioned supervised learning and its connection to offline rl. *arXiv preprint arXiv:2202.04478*, 2022.
- [3] S. Park, D. Ghosh, B. Eysenbach, and S. Levine. Hiql: Offline goal-conditioned rl with latent states as actions. In A. Oh, T. Naumann, A. Globerson, K. Saenko, M. Hardt, and S. Levine, editors, *Advances in Neural Information Processing Systems*, volume 36, pages 34866–34891. Curran Associates, Inc., 2023. URL [https://proceedings.neurips.cc/paper\\_files/paper/2023/file/6d7c4a0727e089ed6cdd3151cbe8d8ba-Paper-Conference.pdf](https://proceedings.neurips.cc/paper_files/paper/2023/file/6d7c4a0727e089ed6cdd3151cbe8d8ba-Paper-Conference.pdf).
- [4] Y. J. Ma, S. Sodhani, D. Jayaraman, O. Bastani, V. Kumar, and A. Zhang. Vip: Towards universal visual reward and representation via value-implicit pre-training. *arXiv preprint arXiv:2210.00030*, 2022.
- [5] T. Schaul, D. Horgan, K. Gregor, and D. Silver. Universal value function approximators. In F. Bach and D. Blei, editors, *Proceedings of the 32nd International Conference on Machine Learning*, volume 37 of *Proceedings of Machine Learning Research*, pages 1312–1320, Lille, France, 07–09 Jul 2015. PMLR. URL <https://proceedings.mlr.press/v37/schaul15.html>.
- [6] M. Weissenbacher, S. Sinha, A. Garg, and K. Yoshinobu. Koopman q-learning: Offline reinforcement learning via symmetries of dynamics. In *International conference on machine learning*, pages 23645–23667. PMLR, 2022.
- [7] P. Cheng, X. Zhan, W. Zhang, Y. Lin, H. Wang, L. Jiang, et al. Look beneath the surface: Exploiting fundamental symmetry for sample-efficient offline rl. *Advances in Neural Information Processing Systems*, 36:7612–7631, 2023.
- [8] S. Park, D. Mann, and S. Levine. Dual goal representations, 2025. URL <https://arxiv.org/abs/2510.06714>.
- [9] R. Ni, Z. Pan, and A. H. Qureshi. Physics-informed temporal difference metric learning for robot motion planning. *arXiv preprint arXiv:2505.05691*, 2025.
- [10] H. Ren, R. Ni, and A. H. Qureshi. Physics-informed neural time fields for prehensile object manipulation. In *2025 IEEE/RSJ International Conference on Intelligent Robots and Systems (IROS)*, pages 11327–11334. IEEE, 2025.
- [11] Y. Liu, A. Buynitsky, R. Ni, and A. H. Qureshi. Physics-informed neural motion planning via domain decomposition in large environments. *arXiv preprint arXiv:2506.12742*, 2025.
- [12] R. Ni and A. H. Qureshi. Ntfields: Neural time fields for physics-informed robot motion planning. *arXiv preprint arXiv:2210.00120*, 2022.
- [13] R. Ni and A. H. Qureshi. Physics-informed neural motion planning on constraint manifolds. In *2024 IEEE International Conference on Robotics and Automation (ICRA)*, pages 12179–12185. IEEE, 2024.

- [14] R. Ni and A. H. Qureshi. Progressive learning for physics-informed neural motion planning. *arXiv preprint arXiv:2306.00616*, 2023.
- [15] Y.-H. Lien, P.-C. Hsieh, T.-M. Li, and Y.-S. Wang. Enhancing value function estimation through first-order state-action dynamics in offline reinforcement learning, 2024.
- [16] R. Munos and P. Bourgin. Reinforcement learning for continuous stochastic control problems. In M. Jordan, M. Kearns, and S. Solla, editors, *Advances in Neural Information Processing Systems*, volume 10. MIT Press, 1997. URL [https://proceedings.neurips.cc/paper\\_files/paper/1997/file/186a157b2992e7daed3677ce8e9fe40f-Paper.pdf](https://proceedings.neurips.cc/paper_files/paper/1997/file/186a157b2992e7daed3677ce8e9fe40f-Paper.pdf).
- [17] J. Quer and E. Ribera Borrell. Connecting stochastic optimal control and reinforcement learning. *Journal of Mathematical Physics*, 65(8), 2024.
- [18] M. G. Crandall and P.-L. Lions. Viscosity solutions of hamilton-jacobi equations. *Transactions of the American mathematical society*, 277(1):1–42, 1983.
- [19] S. Park, K. Frans, D. Mann, B. Eysenbach, A. Kumar, and S. Levine. Horizon reduction makes rl scalable. *arXiv preprint arXiv:2506.04168*, 2025.
- [20] L. P. Kaelbling. Learning to achieve goals. In *IJCAI*, volume 2, pages 1094–8, 1993.
- [21] S. Levine, A. Kumar, G. Tucker, and J. Fu. Offline reinforcement learning: Tutorial, review, and perspectives on open problems, 2020. URL <https://arxiv.org/abs/2005.01643>.
- [22] M. Andrychowicz, F. Wolski, A. Ray, J. Schneider, R. Fong, P. Welinder, B. McGrew, J. Tobin, O. Pieter Abbeel, and W. Zaremba. Hindsight experience replay. In I. Guyon, U. V. Luxburg, S. Bengio, H. Wallach, R. Fergus, S. Vishwanathan, and R. Garnett, editors, *Advances in Neural Information Processing Systems*, volume 30. Curran Associates, Inc., 2017. URL [https://proceedings.neurips.cc/paper\\_files/paper/2017/file/453fadbd8a1a3af50a9df4df899537b5-Paper.pdf](https://proceedings.neurips.cc/paper_files/paper/2017/file/453fadbd8a1a3af50a9df4df899537b5-Paper.pdf).
- [23] Y. Chebotar, K. Hausman, Y. Lu, T. Xiao, D. Kalashnikov, J. Varley, A. Irpan, B. Eysenbach, R. Julian, C. Finn, and S. Levine. Actionable models: Unsupervised offline reinforcement learning of robotic skills, 2021. URL <https://arxiv.org/abs/2104.07749>.
- [24] J. Peters, K. Mulling, and Y. Altun. Relative entropy policy search. *Proceedings of the AAAI Conference on Artificial Intelligence*, 24(1):1607–1612, Jul. 2010.
- [25] X. B. Peng, A. Kumar, G. Zhang, and S. Levine. Advantage-weighted regression: Simple and scalable off-policy reinforcement learning, 2019. URL <https://arxiv.org/abs/1910.00177>.
- [26] I. Kostrikov, A. Nair, and S. Levine. Offline reinforcement learning with implicit q-learning, 2021. URL <https://arxiv.org/abs/2110.06169>.
- [27] H. Ahn, H. Choi, J. Han, and T. Moon. Option-aware temporally abstracted value for offline goal-conditioned reinforcement learning. *arXiv preprint arXiv:2505.12737*, 2025.
- [28] T. Wang, A. Torralba, P. Isola, and A. Zhang. Optimal goal-reaching reinforcement learning via quasimetric learning. In *International Conference on Machine Learning*, pages 36411–36430. PMLR, 2023.
- [29] B. Eysenbach, T. Zhang, S. Levine, and R. R. Salakhutdinov. Contrastive learning as goal-conditioned reinforcement learning. *Advances in Neural Information Processing Systems*, 35: 35603–35620, 2022.
- [30] R. Munos. A convergent reinforcement learning algorithm in the continuous case based on a finite difference method. In *IJCAI (2)*, pages 826–831, 1997.

- [31] A. Shilova, T. Delliaux, P. Preux, and B. Raffin. *Learning HJB Viscosity Solutions with PINNs for Continuous-Time Reinforcement Learning*. PhD thesis, Inria Lille-Nord Europe, CRISTAL-Centre de Recherche en Informatique, Signal . . . , 2024.
- [32] S. Matada, L. Bhan, Y. Shi, and N. Atanasov. Generalizable motion planning via operator learning. *arXiv preprint arXiv:2410.17547*, 2024.
- [33] H. Viswanath, H. C. Nam, J. Berner, A. Anandkumar, and A. Bera. Gradient-free physics-informed operator learning using walk-on-spheres, 2025. URL <https://openreview.net/forum?id=cnMHdAhuod>.
- [34] S. W. Park, K. Lee, and J. Kwon. Neural markov controlled sde: Stochastic optimization for continuous-time data. In *International Conference on Learning Representations*, 2021.
- [35] M. Pereira, Z. Wang, I. Exarchos, and E. A. Theodorou. Learning deep stochastic optimal control policies using forward-backward sdes. *arXiv preprint arXiv:1902.03986*, 2019.
- [36] E. Todorov. Compositionality of optimal control laws. *Advances in neural information processing systems*, 22, 2009.
- [37] H. Wang, T. Zariphopoulou, and X. Y. Zhou. Reinforcement learning in continuous time and space: A stochastic control approach. *Journal of Machine Learning Research*, 21(198):1–34, 2020.
- [38] Y. Jia and X. Y. Zhou. Policy gradient and actor-critic learning in continuous time and space: Theory and algorithms. *Journal of Machine Learning Research*, 23(275):1–50, 2022.
- [39] D. E. Kirk. *Optimal control theory: an introduction*. Courier Corporation, 2004.
- [40] W. H. Fleming and H. M. Soner. *Controlled Markov processes and viscosity solutions*. Springer, 2006.
- [41] B. Goldys and F. Gozzi. Second order parabolic hamilton–jacobi–bellman equations in hilbert spaces and stochastic control:  $L^2$  approach. *Stochastic processes and their applications*, 116(12):1932–1963, 2006.
- [42] V. Nevistic and J. A. Primbs. Constrained nonlinear optimal control: a converse hjb approach. *California Institute of Technology, Pasadena, CA*, 91125:96–021, 1996.
- [43] J. Yong and X. Y. Zhou. *Stochastic controls: Hamiltonian systems and HJB equations*, volume 43. Springer Science & Business Media, 1999.
- [44] M. Hua, M. Lauriere, and E. Vanden-Eijnden. A simulation-free deep learning approach to stochastic optimal control. 2024.
- [45] S. Park, K. Frans, B. Eysenbach, and S. Levine. Ogbench: Benchmarking offline goal-conditioned rl. *arXiv preprint arXiv:2410.20092*, 2024.
- [46] D. Shah, B. Eysenbach, G. Kahn, N. Rhinehart, and S. Levine. Rapid exploration for open-world navigation with latent goal models. *arXiv preprint arXiv:2104.05859*, 2021.
- [47] V. Myers, B. C. Zheng, A. Dragan, K. Fang, and S. Levine. Temporal representation alignment: Successor features enable emergent compositionality in robot instruction following. *arXiv preprint arXiv:2502.05454*, 2025.
- [48] D. Lawson, A. Hugessen, C. Cloutier, G. Berseth, and K. Khetarpal. Self-predictive representations for combinatorial generalization in behavioral cloning. *arXiv preprint arXiv:2506.10137*, 2025.

## A Notations

To promote readability, we provide a table of notations used in Table 4.

Notations	Explanation
<b>Goal-conditional Reinforcement Learning</b>	
$\mathcal{M}$	A Markov decision process (MDP).
$\mathcal{S}$	State space of a Markov decision process.
$\mathcal{A}$	Action space of a Markov decision process.
$s_t$	State at time step $t$ .
$s'$	Generic notation for next state given current state $s$ .
$\mathbf{a}_t$	Action of the agent at time step $t$ .
$r(s_t, \mathbf{g})$	Scalar goal-conditioned reward at state $s_t \in \mathcal{S}$ to reach goal $g \in \mathcal{S}$ .
$p(s_{t+1}   s_t, \mathbf{a}_t)$	System dynamics of an MDP as a state transition probability.
$\pi(\mathbf{a}_t   s_t, \mathbf{g})$	Goal-conditioned policy.
$\Pi$	The space of valid policies.
$\tau$	Trajectory consisting a sequence of state-action pairs $\tau \triangleq (s_0, \mathbf{a}_0, \dots, s_T, \mathbf{a}_T)$ .
$p^\pi(\tau   \cdot)$	A distribution of trajectories conditioned on policy $\pi$ .
$V^\pi(s_t, \mathbf{g})$	Goal-conditioned state value function following policy $\pi$ .
$V^*(s_t, \mathbf{g})$	Optimal Goal-conditioned state value function following policy $\pi^*$ .
<b>Stochastic Optimal Control</b>	
$f(s, \mathbf{a})$	Deterministic component in the state transition dynamics.
$\sigma$	Scalar intensity factor of the jump.
$\mathbf{G}(s)$	Control matrix at state $s$ .
$H(s, \mathbf{a}, \cdot)$	Hamiltonian of the control system.
$c(s, \mathbf{a})$	Running cost in the control system.
$q(s, \cdot)$	Terminal cost in the control system.

Table 4: Table of notations in the paper.

## B Additional Derivations

### B.1 Solution to Optimal Control

Consider a continuous-time dynamical system with dynamics

$$ds_t = b(s_t, \mathbf{a}_t) dt, \quad (8)$$

where  $b(s_t, \mathbf{a}_t)$  is the drift, which may in general depend on the state and control.

The minimum expected cumulative cost to reach a goal state  $\mathbf{g}$  from an initial state  $\mathbf{s}$  is defined by the value function:

$$V^*(\mathbf{s}; \mathbf{g}) = \min_{\pi \in \Pi} \mathbb{E} \left[ \int_0^\infty c(s_t, \mathbf{a}_t) dt + q_f(s_\infty, \mathbf{g}) \mid s_0 = \mathbf{s} \right]. \quad (9)$$

With a control cost,

$$c(s, \mathbf{a}) = q(s) + \frac{1}{2} \|\mathbf{a}\|_2^2, \quad (10)$$

the corresponding *stationary Hamilton-Jacobi-Bellman (HJB) equation* at the vanishing viscosity limit ( $\nu \Delta V$ ) is

$$\min_{\mathbf{a} \in \mathbb{R}^d} \left[ c(s, \mathbf{a}) + (\nabla_s V^*(s; \mathbf{g}))^\top b(s, \mathbf{a}) + \nu \Delta V^*(s; \mathbf{g}) \right] = 0, \quad \Delta V^* = \text{Tr}(\nabla^2 V^*). \quad (11)$$

The expression inside the minimization defines the *Hamiltonian*:

$$H(s, \mathbf{a}, V^*) = c(s, \mathbf{a}) + (\nabla_s V^*(s; \mathbf{g}))^\top \mathbf{a} + \nu \Delta V^*(s; \mathbf{g}). \quad (12)$$

Minimizing  $H$  with respect to  $\mathbf{a}$  yields the *optimal control*:

$$\mathbf{a}^*(\mathbf{s}) = \arg \min_{\mathbf{a}} H(\mathbf{s}, \mathbf{a}, V^*), \quad (13)$$

which defines the optimal policy  $\pi^*(\mathbf{a}|\mathbf{s}) = \delta(\mathbf{a} - \mathbf{a}^*(\mathbf{s}))$ .

Substituting  $\mathbf{a}^*(\mathbf{s})$  back into the Hamiltonian gives the residual under the optimal policy:

$$H(\mathbf{s}, \mathbf{a}^*, V^*) = q(\mathbf{s}) - \frac{1}{2} \|\nabla_{\mathbf{s}} V^*(\mathbf{s}; \mathbf{g})\|_2^2 + \nu \Delta V^*(\mathbf{s}; \mathbf{g}). \quad (14)$$

## B.2 Derivation of Linearized HJB Hamiltonian

We express the gradient and Hessian of the value function  $V^*(\mathbf{s}, \mathbf{g})$  in terms of the desirability function  $\Psi^*(\mathbf{s}, \mathbf{g})$  using the standard linearly solvable control transformation  $V^* = -2\nu \log \Psi^*$ :

$$\begin{aligned} \nabla_{\mathbf{s}} V^*(\mathbf{s}, \mathbf{g}) &= -2\nu \frac{\nabla_{\mathbf{s}} \Psi^*(\mathbf{s}, \mathbf{g})}{\Psi^*(\mathbf{s}, \mathbf{g})}, \\ \nabla_{\mathbf{s}}^2 V^*(\mathbf{s}, \mathbf{g}) &= -2\nu \left( \frac{\nabla_{\mathbf{s}}^2 \Psi^*(\mathbf{s}, \mathbf{g})}{\Psi^*(\mathbf{s}, \mathbf{g})} - \frac{\nabla_{\mathbf{s}} \Psi^*(\mathbf{s}, \mathbf{g}) (\nabla_{\mathbf{s}} \Psi^*(\mathbf{s}, \mathbf{g}))^\top}{(\Psi^*(\mathbf{s}, \mathbf{g}))^2} \right) \end{aligned} \quad (15)$$

Substituting these expressions into the Hamiltonian under the optimal policy in equation 3:

$$\begin{aligned} H_{\text{lin}}(\mathbf{s}, \mathbf{a}^*, \Psi^*) &= q(\mathbf{s}) - \frac{1}{2} \|\nabla_{\mathbf{s}} V^*(\mathbf{s}, \mathbf{g})\|_2^2 + \nu \Delta V^*(\mathbf{s}, \mathbf{g}) \\ &= q(\mathbf{s}) - \frac{1}{2} \left\| -2\nu \frac{\nabla_{\mathbf{s}} \Psi^*}{\Psi^*} \right\|_2^2 + \nu \left[ -2\nu \left( \frac{\Delta \Psi^*}{\Psi^*} - \frac{\|\nabla_{\mathbf{s}} \Psi^*\|_2^2}{(\Psi^*)^2} \right) \right] \\ &= q(\mathbf{s}) - 2\nu^2 \frac{\|\nabla_{\mathbf{s}} \Psi^*\|_2^2}{(\Psi^*)^2} - 2\nu^2 \left( \frac{\Delta \Psi^*}{\Psi^*} - \frac{\|\nabla_{\mathbf{s}} \Psi^*\|_2^2}{(\Psi^*)^2} \right) \\ &= q(\mathbf{s}) - 2\nu^2 \frac{\Delta \Psi^*(\mathbf{s}, \mathbf{g})}{\Psi^*(\mathbf{s}, \mathbf{g})}. \end{aligned} \quad (16)$$

Thus, the nonlinear Hamiltonian in terms of  $V^*$  is transformed into a *linear form in  $\Psi^*$* , which simplifies analysis and computation in linearly solvable optimal control.

## B.3 Feynman-Kac Formula Yields an Upper Bound on the Optimal State Value

The Feynman-Kac formula expresses the desirability function  $\Psi^*(\mathbf{s}, \mathbf{g})$  as a conditional expectation over the next state  $\mathbf{s}'$ :

$$\Psi^*(\mathbf{s}, \mathbf{g}) = \mathbb{E}_{\mathbf{s}' \sim p(\mathbf{s}'|\mathbf{s}, \mathbf{a})} \left[ e^{-\frac{\Delta t}{2\nu^2} q(\mathbf{s})} \Psi^*(\mathbf{s}', \mathbf{g}) \right]. \quad (17)$$

Taking the logarithm and applying *Jensen's inequality* gives

$$\begin{aligned} \log \Psi^*(\mathbf{s}, \mathbf{g}) &= \log \mathbb{E}_{p(\mathbf{s}'|\mathbf{s}, \mathbf{a})} \left[ e^{-\frac{\Delta t}{2\nu^2} q(\mathbf{s})} \Psi^*(\mathbf{s}', \mathbf{g}) \right] \\ &= -\frac{\Delta t}{2\nu^2} q(\mathbf{s}) + \log \mathbb{E}_{p(\mathbf{s}'|\mathbf{s}, \mathbf{a})} \Psi^*(\mathbf{s}', \mathbf{g}) \\ &\geq -\frac{\Delta t}{2\nu^2} q(\mathbf{s}) + \mathbb{E}_{p(\mathbf{s}'|\mathbf{s}, \mathbf{a})} \log \Psi^*(\mathbf{s}', \mathbf{g}). \end{aligned} \quad (18)$$

Substituting the transformation  $V^*(\mathbf{s}, \mathbf{g}) = -2\nu \log \Psi^*(\mathbf{s}, \mathbf{g})$ , we obtain

$$-\frac{V^*(\mathbf{s}, \mathbf{g})}{2\nu} \geq -\frac{\Delta t}{2\nu^2} q(\mathbf{s}) + \mathbb{E}_{p(\mathbf{s}'|\mathbf{s}, \mathbf{a})} \left[ -\frac{V^*(\mathbf{s}', \mathbf{g})}{2\nu} \right], \quad (19)$$

or equivalently, multiplying both sides by  $-2\nu$  (which reverses the inequality):

$$V^*(\mathbf{s}, \mathbf{g}) \leq \frac{\Delta t}{\nu} q(\mathbf{s}) + \mathbb{E}_{p(\mathbf{s}'|\mathbf{s}, \mathbf{a})} [V^*(\mathbf{s}', \mathbf{g})]. \quad (20)$$

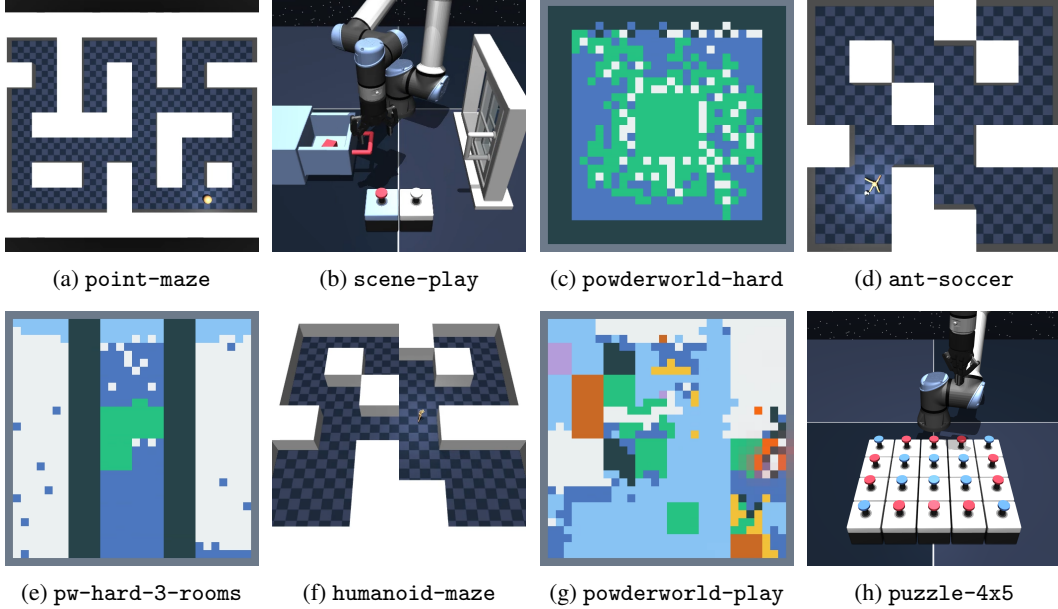


Figure 5: **Benchmark Suite from OGBench** We evaluate our method across a wide spectrum of offline GCRL tasks, ranging from standard geometric navigation (point/ant/humanoid-maze) and high-dimensional manipulation (scene-play, puzzle), to the highly stochastic, pixel-based physics of powderworld. This diversity tests the agent’s ability to handle varying degrees of state dimensionality, transition stochasticity, and dynamic complexity.

This establishes a *discrete-time upper bound* on the optimal state value in terms of the desirability function and the running cost, fully consistent with the linearized HJB PDE

$$-\Delta\Psi(\mathbf{s}, \mathbf{g}) + \frac{1}{2\nu^2}q(\mathbf{s})\Psi(\mathbf{s}, \mathbf{g}) = 0.$$

## C Implementation and Hyperparameters

Our experimental framework is built upon the OGBench benchmark suite [45]. For the dual representation baselines, we follow [8] to compute temporal distances by randomly sampling 64 anchor states and executing a breadth-first search (BFS). The vector of distances to these anchors serves as the dual representation. We train a goal-conditioned DQN using a sparse reward function ( $-1$  for non-goal states,  $0$  for the goal). Agents are trained for  $10^6$  steps, and the argmax policy is evaluated over 15 episodes per task. A full list of hyperparameters, including the specific hindsight relabeling ratios (curriculum, geometric, trajectory, and random), is provided in Table 8.

**Reward.** As per OGBench, we define a sparse binary reward function for training GCVF:  $r(\mathbf{s}, \mathbf{g}) = 0$  if  $\mathbf{s} = \mathbf{g}$ , and  $-1$  otherwise. Under this formulation, the optimal value function encodes the discounted temporal distance:

$$V^*(\mathbf{s}, \mathbf{g}) = -\frac{1 - \gamma^{d^*(\mathbf{s}, \mathbf{g})}}{1 - \gamma}$$

Following the dual-goal-representations [8], we approximate this value using the inner product of the learned representations,  $f(\psi(\mathbf{s}), \phi(\mathbf{g})) = \psi(\mathbf{s})^\top \phi(\mathbf{g})$ .

**Evaluation.** We report performance based on the average success rate over the final three training epochs. This corresponds to the window covering 800K–1M gradient steps. Evaluation aggregates results from 50 episodes (state-based) across the five designated evaluation goals.

**Hyperparameters and Architecture.** Complete hyperparameter configurations are listed in Table 9. Consistent with OGBench, we apply Layer Normalization to all neural network layers, with the

exception of the policy networks in GCIVL and CRL baselines. We use the Adam optimizer and GELU activation functions throughout.

Table 5: Hyperparameters for experiments.

Hyperparameter	Value
Gradient steps	$10^6$ (state-based), $5 \times 10^5$ (pixel-based)
Optimizer	Adam
Learning rate	0.0003
Batch size	1024 (state-based), 256 (pixel-based)
MLP size	[512, 512, 512]
Nonlinearity	GELU
Target network update rate	0.005
Discount factor $\gamma$	0.99 (default), 0.995 (humanoidmaze, antmaze-giant)
Goal representation dimensionality $N$	256 (default), 64 (pointmaze)
Dual representation’s GCIQL expectile $\kappa$	0.7 (default), 0.9 (navigate)
Size of random walk neighborhood $K$	10
Eikonal Speed Type	Constant, exactly defined in [1]
Noise standard deviation $\nu$	0.01
VIB $\beta$	0.001 (default), 0.003 (pointmaze, antmaze-large)
Rep ( $p_{\mathcal{D}}^{\text{cur}}, p_{\mathcal{D}}^{\text{geom}}, p_{\mathcal{D}}^{\text{traj}}, p_{\mathcal{D}}^{\text{rand}}$ ) ratio (Dual)	(0.2, 0.5, 0, 0.3)
Rep ( $p_{\mathcal{D}}^{\text{cur}}, p_{\mathcal{D}}^{\text{geom}}, p_{\mathcal{D}}^{\text{traj}}, p_{\mathcal{D}}^{\text{rand}}$ ) ratio (TRA, BYOL- $\gamma$ )	(0, 1, 0, 0)
Downstream GCIVL expectile	0.9
Downstream policy extraction hyperparameters	Identical to OGBench
Downstream policy ( $p_{\mathcal{D}}^{\text{cur}}, p_{\mathcal{D}}^{\text{geom}}, p_{\mathcal{D}}^{\text{traj}}, p_{\mathcal{D}}^{\text{rand}}$ ) ratio	(0, 0, 1, 0)
Downstream value ( $p_{\mathcal{D}}^{\text{cur}}, p_{\mathcal{D}}^{\text{geom}}, p_{\mathcal{D}}^{\text{traj}}, p_{\mathcal{D}}^{\text{rand}}$ ) ratio (default)	(0.2, 0.5, 0, 0.3)
Downstream value ( $p_{\mathcal{D}}^{\text{cur}}, p_{\mathcal{D}}^{\text{geom}}, p_{\mathcal{D}}^{\text{traj}}, p_{\mathcal{D}}^{\text{rand}}$ ) ratio (CRL)	(0, 1, 0, 0)

## D Ablations

Table 6: **HIGH-DIMENSIONAL STOCHASTIC DYNAMICS (POWDERWORLD)**. Overall results on pixel-based tasks where environment dynamics are highly stochastic (e.g., sand piling, fire spreading). Since raw pixel perturbation is infeasible, GCIVL-PIXEL-FK enforces the viscous consistency condition via sampling in the *Impala* encoder’s latent embedding space.

ENVIRONMENT	GCIVL-PIXEL	GCIVL-PIXEL-EIK	GCIVL-PIXEL-FK (OURS)
powderworld-easy	<b>99 ± 1</b>	<b>99 ± 1</b>	<b>99 ± 1</b>
powderworld-medium	50 ± 4	<b>61 ± 4</b>	<b>62 ± 7</b>
powderworld-hard	4 ± 3	7 ± 3	<b>10 ± 2</b>

In this section we discuss two key ablations for our proposed approach. Our method depends on two key variables - number of neighborhoods  $K$  and the scale  $\nu$ . We present the contour plots to showcase the changes in the learned value function. We present the results in Table 3b.

As shown in Table 3b, increasing the sample budget  $K$  yields a performance improvement from 57% to 77% between 1 and 5 walks, after which the success rate saturates. While the qualitative structure of the value landscape appears stable even with a single sample (Figure 6), the quantitative gap suggests that reducing the variance of the Feynman-Kac estimator is beneficial for policy extraction. In contrast, the method shows greater sensitivity to the Laplacian scale ( $\nu$ ). Lower values ( $\nu \leq 10^{-3}$ ) result in a marked drop in performance (Table 3b). This behavior is visually explained in Figure 7: a larger scale is necessary to smooth the value function across geometrical bottlenecks (Figure 7a). When the scale is too small (Figure 7d), the regularization becomes strictly local, causing the value contours to align with obstacles rather than reflecting the global geodesic structure. By choosing a small  $K \leq 20$ , we observe no significant changes in wall-clock time for training.

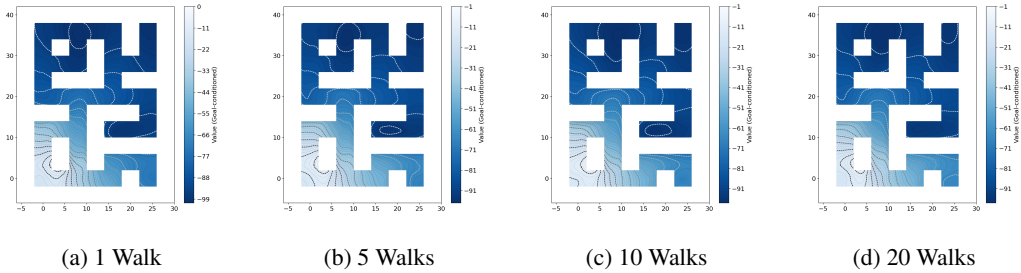


Figure 6: Ablation on the number of random walks sampled for the stochastic regularizer. We observe no sharp visible changes in the learned value contours as the number of walks increases. However, for 1-walk, we observe worse performance

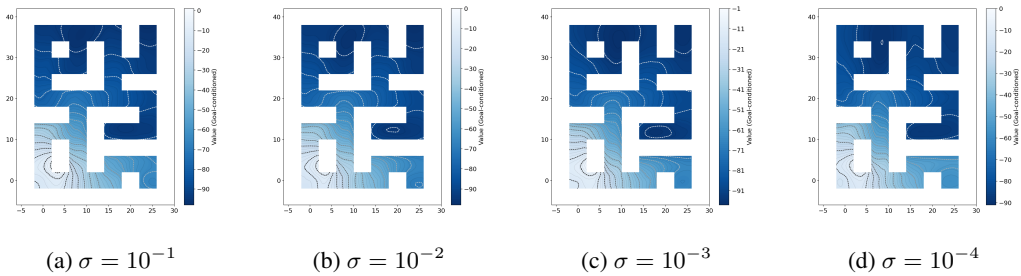


Figure 7: Ablation on the random walk step size (neighborhood size). Unlike the number of walks, the step size significantly affects the learned geometry. With a sufficiently large neighborhood (a), the contours correctly identify the global structure. However, as the step size decreases to  $10^{-4}$  (d), the random walks become too local to bridge obstacles. This causes the value contours to collapse parallel to the walls, creating local minima and failing to capture the geodesic distance.

## D.1 Comparing Success Rates on OGBench

We evaluate our method against two competitive baselines: the Eikonal dual-goal representation (Dual), which enforces a first-order Eikonal constraint, and the Variational Information Bottleneck (VIB) baseline. Figure 8 presents the learning curves across eight challenging environments from the OGBench suite, including navigation, manipulation, and high-dimensional locomotion tasks.

As illustrated in Figure 8, enforcing the stochastic Feynman-Kac consistency condition yields consistent performance gains. In geometrically complex navigation tasks such as *AntMaze Medium* and *PointMaze Large*, our method (Teal) converges significantly faster than the baselines, suggesting that the stochastic regularization effectively smooths the value landscape and prevents the agent from getting stuck in local minima inherent to the Eikonal formulation. Notably, in the *PointMaze Teleport* task, where the state transitions are discontinuous, the baseline methods struggle to propagate value information across the teleportation pads. In contrast, our approach maintains robust performance, validating the hypothesis that the stochastic term provides a necessary “blurring” effect that bridges disconnected regions of the state space.

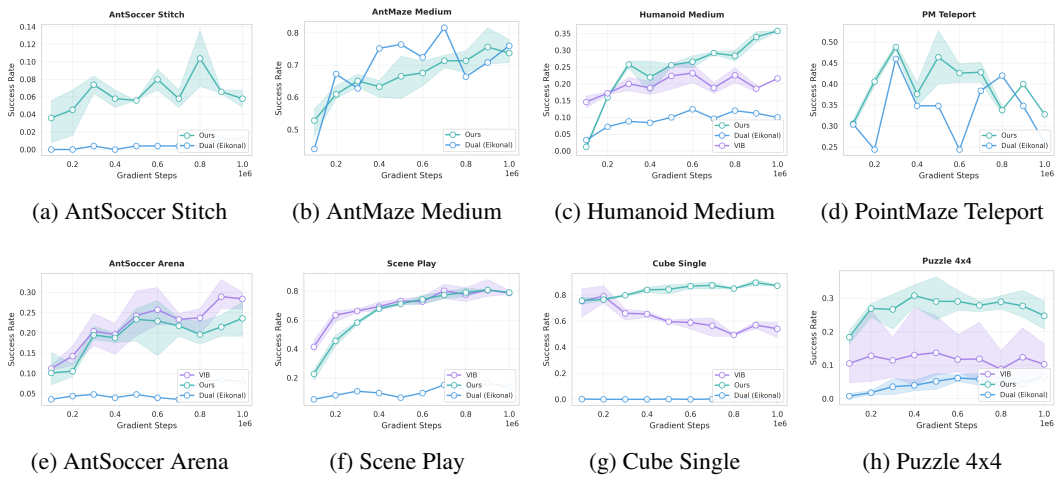


Figure 8: **Learning Curves on OGBench.** We compare our proposed stochastic regularization (Teal) against the standard Dual Eikonal baseline (Blue) and VIB (Purple). The curves report the average success rate over 3 random seeds, with shaded regions indicating the standard error. Our method consistently achieves faster convergence and higher asymptotic performance, particularly in “Stitch” tasks where the agent must combine suboptimal prior data to solve novel goals.